SANDIA REPORT

SAND2000-2769 Unlimited Release Printed November 2000

Micromechanical Failure Analyses for Finite Element Polymer Modeling

R. S. Chambers, E. D. Reedy, Jr., C. S. Lo, D. B. Adolf, and T. R. Guess

Prepared by
Sandia National Laboratories
Albuquerque, New Mexico 87185 and Livermore, California 94550

Sandia is a multiprogram laboratory operated by Sandia Corporation, a Lockheed Martin Company, for the United States Department of Energy under Contract DE-AC04-94AL85000.

Approved for public release; further dissemination unlimited.



Issued by Sandia National Laboratories, operated for the United States Department of Energy by Sandia Corporation.

NOTICE: This report was prepared as an account of work sponsored by an agency of the United States Government. Neither the United States Government, nor any agency thereof, nor any of their employees, nor any of their contractors, subcontractors, or their employees, make any warranty, express or implied, or assume any legal liability or responsibility for the accuracy, completeness, or usefulness of any information, apparatus, product, or process disclosed, or represent that its use would not infringe privately owned rights. Reference herein to any specific commercial product, process, or service by trade name, trademark, manufacturer, or otherwise, does not necessarily constitute or imply its endorsement, recommendation, or favoring by the United States Government, any agency thereof, or any of their contractors or subcontractors. The views and opinions expressed herein do not necessarily state or reflect those of the United States Government, any agency thereof, or any of their contractors.

Printed in the United States of America. This report has been reproduced directly from the best available copy.

Available to DOE and DOE contractors from

U.S. Department of Energy
Office of Scientific and Technical Information
P.O. Box 62
Oak Ridge, TN 37831

Telephone: (865)576-8401 Facsimile: (865)576-5728

E-Mail: reports@adonis.osti.gov

Online ordering: http://www.doe.gov/bridge

Available to the public from
U.S. Department of Commerce
National Technical Information Service
5285 Port Royal Rd
Springfield, VA 22161

Telephone: (800)553-6847 Facsimile: (703)605-6900

E-Mail: <u>orders@ntis.fedworld.gov</u>

Online order: http://www.ntis.gov/ordering.htm



SAND2000-2769 Unlimited Release Printed November 2000

Micromechanical Failure Analyses for Finite Element Polymer Modeling

R. S. Chambers, E. D. Reedy, Jr. and C. S. Lo Material Mechanics

D. B. Adolf Organic Materials Aging and Reliability

> T. R. Guess Organic Materials

Sandia National Laboratories P. O. Box 5800 Albuquerque, NM 87185-0847

Abstract

Polymer stresses around sharp corners and in constrained geometries of encapsulated components can generate cracks leading to system failures. Often, analysts use maximum stresses as a qualitative indicator for evaluating the strength of encapsulated component designs. Although this approach has been useful for making relative comparisons screening prospective design changes, it has not been tied quantitatively to failure. Accurate failure models are needed for analyses to predict whether encapsulated components meet life cycle requirements. With Sandia's recently developed nonlinear viscoelastic polymer models, it has been possible to examine more accurately the local stress-strain distributions in zones of likely failure initiation looking for physically based failure mechanisms and continuum metrics that correlate with the cohesive failure event. This study has identified significant differences between rubbery and glassy failure mechanisms that suggest reasonable alternatives for cohesive failure criteria and metrics. Rubbery failure seems best characterized by the mechanisms of finite extensibility and appears to correlate with maximum strain predictions. Glassy failure, however, seems driven by cavitation and correlates with the maximum hydrostatic tension. Using these metrics, two three-point bending geometries were tested and analyzed under variable loading rates, different temperatures and comparable mesh resolution (i.e., accuracy) to make quantitative failure predictions. The resulting predictions and observations agreed well suggesting the need for additional research.

In a separate, additional study, the asymptotically singular stress state found at the tip of a rigid, square inclusion embedded within a thin, linear elastic disk was determined for uniform cooling. The singular stress field is characterized by a single stress intensity factor K_a , and the applicable K_a calibration relationship has been determined for both fully bonded and unbonded inclusions. A lack of interfacial bonding has a profound

effect on inclusion-tip stress fields. A large radial compressive stress is generated in front of the inclusion tip when the inclusion is well bonded, whereas a large tensile hoop stress is generated when the inclusion is unbonded, and frictionless sliding is allowed. Consequently, an epoxy disk containing an unbonded inclusion appears more likely to crack when cooled than a disk containing a fully bonded inclusion. A limited number of tests have been carried out to determine if encapsulant cracking can be induced by cooling a specimen fabricated by molding a square, steel insert within a thin, epoxy disk. Test results are in qualitative agreement with analysis. Cracks developed only in disks with mold-released inserts, and the tendency for cracking increased with inclusion size.

Table of Contents

I.	Introduction	n	1		
II.	Approach to Developing Cohesive Failure Criterion				
III.	Viscoelastic Modeling				
IV.	Failure Test Geometries				
V.	Failure Hypotheses				
VI.	Failure Metrics and Modeling Approach				
VII.	Rubbery Analyses				
VIII.	Glassy Analyses				
IX.	Finite Element Meshing and Modeling Issues				
X.	Summary				
XI.	Future Direction				
XII.	References				
APPENDIX A		Fracture Toughness of 828/DEA Epoxy – Effects of Loading Rate and Test Temperature			
APPENDIX B		Rigid Square Inclusion Embedded within an Epoxy Disk: Asymptotic Stress Analysis			

I. Introduction

Thermosets are used to encapsulate a variety of weapon components with the encapsulant serving to provide structural integrity, moisture and vibration protection and high voltage isolation for delicate parts. Polymer stresses around sharp corners and in constrained geometries of encapsulated components can generate cracks leading to system failures. Often, analysts use maximum stresses as a qualitative indicator for evaluating the strength of encapsulated component designs. Although this approach has been useful for making relative comparisons screening prospective design changes, it is not applied as an absolute definition of failure. In the current climate which demands more for less (i.e., higher performance and greater surety at lower costs), it is becoming more important to make accurate life cycle predictions and assign quantitatively meaningful margins of safety. To do so, accurate polymer failure models are needed. Ideally, these models should be broadly applicable under general operational environments affecting temperature, loading, geometry, and material aging. Moreover, it is extremely advantageous if they interface directly with the finite element codes employed in engineering analyses. Although thermosets can fail adhesively (i.e., at material interfaces) as well as cohesively (i.e., within the same material), this project has focussed exclusively on cohesive failure events with the belief that things learned here also will contribute to the study of adhesion. Specifically, two different topics have been considered: the first looking at failure mechanisms and the second looking at failure analyses. Hence, the dual purpose of this project was:

- 1) to use accurate descriptions of nonlinear viscoelastic stress/strain fields in cohesive failure zones to identify failure mechanisms and look for continuum material-based metrics for potentially new failure criteria,
- 2) to develop a failure analysis for cohesive cracking from the tip of a sharp-cornered, encapsulated inclusion using an approach that is analogous to linear elastic fracture mechanics, except here the critical value of the stress intensity factor is associated with a corner discontinuity rather than a crack tip.

Although this work originally was proposed as a two year program, it was granted a one year extension to make clear the distinctions between rubbery and glassy failure. The corner toughness problem (item 2 above) was investigated by E. D. Reedy, Jr., and T. R. Guess during years one and two. Their results were documented separately and are included in Appendix B for completeness. The nonlinear viscoelastic analyses and work in cohesive failure mechanisms (item 1) are presented in the subsequent text of this report. This work was conducted by D. B. Adolf and R. S. Chambers with some fracture toughness tests done by T. R. Guess and M. E. Stavig and some analyses performed by C. S. Lo (particularly the parallel computing effort).

II. Approach to Developing a Cohesive Failure Criterion

Linear elastic fracture mechanics is used to predict crack growth when there is small scale yielding at the tip of a crack (i.e., process zone is small). This macro-

approach to failure foregoes the complexity of the actual material behavior at the crack tip and defines a toughness parameter ($K_{\rm Ic}$) as the basis for determining when the crack will grow [1]. Although this greatly simplifies the failure analyses, it does so at the expense of material testing which must characterize the critical toughness for the multiplicity of conditions likely to be seen in a service life (e.g., modes of loading, variable loading rates, temperatures, extents of reaction, etc.).

This project takes a different view, opting to look explicitly at the details of the actual epoxy behavior in local regions of high stress concentration. The continuum stresses and strains are used to construct quantitative cohesive failure metrics (e.g., maximum strain, hydrostatic tensile stress, etc.) to serve as indicators for the specific physical failure mechanisms (e.g., finite extensibility, cavitation) that are being proposed. The failure mechanisms and criteria then are evaluated by performing both detailed analyses and failure tests on different sample geometries under to a variety of conditions to see whether the predictions correlate with observed failures. If such an approach works, it not only identifies physical failure mechanisms, but it also relates the continuum material response to those physical failure mechanisms in a predictable way. Moreover, it then can be implemented directly in finite element analyses providing a more generally applicable capability for predicting failure, one that is not limited to "small scale yielding". Although the idea of analyzing crack-tip stresses in search of a failure criterion is not new, the approach that was taken in this project is new for the following reasons:

- 1) The stress analyses incorporated the right material physics. Polymers are nonlinear viscoelastic materials. A validated nonlinear viscoelastic material model based on large deformation mechanics with the proper finite strain measure (Hencky strain) was used.
- 2) The failure tests were performed on non-singular geometries (i.e., samples with notches not sharp cracks) making finite element solutions well behaved and convergence more readily attainable.
- 3) Parallel processing was used to perform these computationally taxing analyses.

III. Viscoelastic Modeling

Recent advances in polymer modeling at Sandia National Laboratories have led to the development and validation of linear and nonlinear viscoelastic material models for Sandia's encapsulants (to be published separately). The constitutive equations also have been implemented in the JAS3D finite element code [2]. With these tools, it is now possible to analyze fully three dimensional geometries under arbitrary loading conditions to predict detailed stress and deformation histories as functions of time, temperature, and aging (physical and chemical). Figures 1-3 provide comparisons between the model predictions and experimental measurements conducted with the Epon 828/DEA unfilled epoxy system for three distinctly different types of tests: uniaxial compression/tension, volume straining under cyclic thermal histories, and enthalpy relaxation (aged and unaged). The host of physics now predictable encompasses a full range of polymer behavior: yielding under arbitrary loading, relaxation in stress and volume, physical

aging, etc. Unfilled Epon 828/DEA was selected for all the experiments and analyses performed under this project in developing the cohesive failure criteria.

IV. Failure Test Geometries

All failure tests were conducted with a three-point bending specimen. The baseline sample geometry was a rectangular bar (length 4", depth w=0.5", and thickness=0.25") with a 2" span between supports. The linear elastic fracture toughness (documented in Appendix A) was measured using edge-cracked specimens. However, in developing the cohesive failure criteria, two types of notched (non-singular) geometries were used. The first was a narrow-notched sample having a 0.004" (100 micron) notch radius yielding a 0.008" total slot width. The second geometry contained a semi-circular, cut-out of constant radius centered on the bottom edge of the beam. For the latter geometry, multiple test samples were created using cutting diameters equal to 0.125", 0.25", 0.50" and 0.69". The two three-point bending test geometries are illustrated in Figure 4.

V. Failure Hypotheses

Thermosets are viscoelastic materials which exhibit both glassy and rubbery behavior. This is readily apparent from a simple shear stress relaxation test in which a thermoset (e.g., Epon 828/DEA) is subjected to an instantaneously applied constant shear strain, and the shear stress is observed to decay over time. The glassy modulus which is computed by dividing the initial, short-time shear stress by the constant shear strain is seen to be about 100 times larger than the long-time, rubbery (equilibrium) modulus. This disparity in the magnitude of the moduli is related directly to the internal load carrying mechanisms. The rubbery modulus arises from intermolecular (chain extension) forces. Although these also are present in the glass, they are not the dominant load carrying mechanism. Instead, it is the intramolecular (van der Waals) forces which carry most of the load in the glass. These facts are important for distinguishing why the glass behaves differently from the rubber.

In addition to the observed differences in moduli between the glassy and rubbery regimes of thermosets, there also are differences in their observed failures. Under identical loadings, the rubber fails first even though the stresses and strains are lower than those in the glass. Moreover, in a compression test, the rubber tends to shatter into hundreds of small pieces whereas the glass internally cracks but remains in tact. This suggests that the cohesive failure mechanism of the glass is very likely different from that of the rubber.

Influenced by the data and the lore of the polymer community, two distinctly different failure hypotheses were proposed, one for the rubber and one for the glass. Since the physical load carrying mechanism in the rubber comes from stretching the underlying global polymer network, a finite extensibility criterion was suggested. Under this view of failure, the network strains gradually are stretched until they reach some physical limit. When all chains have been extended such that there are no more extensional degrees of freedom, the chains rupture and the sample fails catastrophically.

To a certain extent, this same picture also carries over into glassy failure. When a glass is stretched, the network chains likewise are stretched, ultimately to the same limit. The difference, however, is that the glass provides a second more dominant load carrying capability. Although the chains in the glass may break as they did in the rubber, the glass has intramolecular (van der Waals) forces which continue to carry the load. This means that chain rupture is not catastrophic. Rather, the loading can continue until another failure mechanism occurs. The fact that glassy failure also is an abrupt phenomenon implies that some critical event takes place well after the chain limit has been attained. One such possibility is a cavitation event whereby a "void" suddenly pops into a domain of high stress concentration unleashing a catastrophic material instability. This is the glassy failure mechanism that was chosen for evaluation.

VI. Failure Metrics and Modeling Approach

Having proposed failure mechanisms for the rubber (finite extensibility) and the glass (cavitation), there remains the task of identifying appropriate failure metrics to associate with the proposed physical failure mechanisms. These metrics are quantities that are obtained from a detailed nonlinear viscoelastic analysis of a failure test and that serve as quantitative indicators which directly correlate with the observed failure events. For the finite extensibility criterion in rubbery failure, a maximum principal strain parameter was selected. A maximum hydrostatic tensile stress was chosen as the indicator of a cavitation failure in the glass. Both metrics, of course, must be evaluated with experimental data to determine their suitability.

There still remains the task of determining whether any of this actually works. To do so, first some failure tests were performed and analyzed to see if the chosen failure metrics performed consistently. This requires one to be able to pick a maximum strain criterion for rubbery failure which falls within the reasonable data spread of the observed test results. Likewise, this must be done for the maximum hydrostatic tensile stress in predicting glassy cavitation. Once the criteria have been selected, then they can be used to predict failures in other tests varying things like loading rate, geometry or temperature. If the failure metrics generally correlate with the observed failures, then there is evidence that the underlying physical failure mechanics and metrics are reasonable, and a finite element based failure prediction is achievable.

VII. Rubbery Analyses

The rubbery failure tests with the semi-circular notched samples loaded in three-point bending were analyzed first. To ensure rubbery behavior, these tests were conducted at 120C which is about 50 degrees above glass transition (Tg=68C). Figure 5 contains a painted color contour plot of the maximum strain taken from the sample with the 0.50" diameter notch. As one would expect from an elastic analysis, the maximum strain occurs on the face of the notch where the stress is concentrated. To determine the critical value of the maximum strain for the finite extensibility failure criterion, finite element analyses of four different failure tests were performed. The simulations were

based on the semi-circular notched geometries with four different notch diameters: 0.125", 0.25", 0.50" and 0.69". From the finite element predictions, plots of the maximum local strain (at the notch edge) as a function of the sample mid-span deflection were generated and are provided in Figure 6. The first task was to determine if the models indicate the existence of a common critical strain that is consistent with the measured displacement to fail in all four geometries. From the experimental scatter in the measured displacements to fail (noted in Figure 6 as error bars), one can identify a corresponding range in potential strains to fail. A common critical strain of 0.24 appears to fall within the data scatter for all the tests as noted in the figure. Using the 24% critical strain as the metric for failure, the loads to fail can be predicted from the analysis results as shown in Figure 7. Since plane strain assumptions were used to analyze the failure tests, one would presume that the predicted strains at failure are probably more accurate that the predicted loads. Plots of the displacement and load to fail as a function of hole diameter are provided in Figures 8 and 9, respectively.

Using the critical strain of 0.24 determined from the failure tests on the circular-notched samples, failure predictions also were made for the narrow-notched (100 micron radius) geometry which more nearly resembles an edge crack. The predicted and measured loads to fail are plotted in Figure 10 as a function of the ratio of notch length to specimen height (a/W). Excellent agreement was obtained. If one treats the narrow notch as a true edge crack and uses the traditional equations for edge-cracked three-point bending samples, an apparent fracture toughness (K_Q) can be computed. This value is plotted in Figure 11 for (a/W) ratios of 0.4, 0.5, 0.6. The important point here is that the apparent toughness is virtually constant as one would expect.

It also is interesting to consider how the load and displacement to fail may be affected by changes in material properties. Batch-to-batch variations, for example, may produce materials with different rubbery moduli. The log-log plots in Figure 12 illustrate this relationship. From these results, it is possible to deduce the dependence of the critical failure strain parameter on the rubbery shear modulus. That relationship is provided in Figure 13.

VIII. Glassy Analyses

To evaluate the glassy failure criterion, the narrow-notched (100 micron radius), three-point bending, room-temperature, failure tests were analyzed under deformations at 0.2"/min. Unlike the rubbery response which was elastic, these solutions reveal significant nonlinear viscoelastic behavior. Evidence for this can be seen in the time and location history of the maximum hydrostatic tensile stress during loading. A painted color plot of the hydrostatic tension zone prior to failure is found in Figure 14. The variation in hydrostatic tensile stress as a function of distance along the symmetry plane measured from the notch tip can be seen in the various time curves of Figure 15. Note that during early times the response is elastic, and the maximum tensile stress occurs at the notch tip. However, as the deformation increases, the material eventually yields pushing the local maximum away from the notch.

Just as was done in the rubbery elastic analyses, here also the failure tests were used to look for a consistent failure criterion, except this time the metric of interest was

the maximum hydrostatic tensile stress. Plots of the predicted maximum hydrostatic tensile stress as a function of mid-span deflection in the room-temperature, three-point bending test are shown in Figure 16 for the three (a/W) geometries. The critical hydrostatic stress that seemed to fall within the data scatter of the measured displacements to fail in all the tests was approximately 125 MPa. Using this value as the failure criterion, one can again make a prediction of the loads and displacements to fail as noted in Figure 17.

The glassy failure analyses were much more difficult to perform. This was due in part to the computational expense of nonlinear viscoelasticity which of course can be offset by running in parallel using more processors. The other issue arises from material yielding. As the elements near the notch tip effectively soften under load, they strain enormously. This can lead to extreme mesh distortion, especially if the strain hardening is not quite right, that requires remeshing. All this further reinforces the need for using the proper strain measure and having a material model validated for large strains. Because of the numerous difficulties and the time constraints on the project, the analyses of the glassy failure tests were not taken all the way to the observed failure deflection. That is the distinction made between the solid and dashed analysis curves shown in Figure 16. The solid lines were plotted directly from the analysis results, and the dashed lines are extrapolations of these curves. Judging from the well behaved character of the analyses, the extrapolations were believed to be realistic. Nevertheless, to verify this assumption, one more step was taken. A second choice for the critical failure metric was selected corresponding to a lower hydrostatic tensile stress, namely 100 MPa. This value was one achieved in all three (a/W) failure test analyses. The idea here was to make failure predictions with both critical stresses (the 125 MPa value and the 100 MPa value). Although it is natural to expect there to be differences in the resulting loads and deflections to fail, one would not expect to see any qualitative differences in the predictive trends. If those do occur, then this casts some doubt on the validity of the aforementioned analysis extrapolations.

In Figure 18, the predicted and measured loads to fail are plotted as a function of the (a/W) ratio for the narrow notched geometries that were tested. Note that predictions were made for both the 125 MPa and the 100 MPa values of the critical hydrostatic tensile stress (glassy failure metric). As expected, the 125 MPa prediction is in line with the data from which it was chosen. The 100 MPa result shows the same trend of decreasing load to fail with increasing (a/W) ratio. The predicted loads to fail are of course less when the critical stress metric is smaller. Figure 19 is a plot of the predicted effective toughness when the narrow notch is treated as an edge crack in a three-point bending test. Again, the important feature here is that both critical stress values result in a predicted apparent toughness that is essentially constant.

To check the validity of the proposed glassy failure mechanism (cavitation) and the associated failure metric (critical hydrostatic tension), other test variations were reviewed. One of these involved changing the beam deflection rate by two orders of magnitude (0.02"/min to 2"/min) to determine whether the sensitivity to rate could be predicted properly. The predicted loads to fail are plotted with the data in Figure 20, and the variation in the apparent toughness is shown in Figure 21. Note that both the loads to fail and toughness decrease with increasing deflection rate. This is consistent with the data. Furthermore, when the failure metric is chosen to be 125 MPa, the predictions are

well within the scatter of the data. If the lower critical hydrostatic tension (100 MPa) is selected instead, the same trends are predicted albeit at lower magnitudes as one would expect.

Temperature sensitivity also was investigated. Tests and analyses were conducted at temperatures of 50, 18 and -50 C loading under deformations imposed at 0.2"/min. The data/analysis comparisons can be seen in Figures 22 and 23. The data show that there is a minimum both in the toughness and in the loads to fail somewhere around room temperature. Although the loads and toughness do appear to increase as one cools from 18 C to -50 C, the magnitude of that increase is much less than the increase observed on heating from 18 C to 50 C (closer to glass transition). The latter increase is predictable as evidenced by the results obtained with the 100 MPa critical stress metric. However, on cooling from 18 C to -50 C, the model predicts a nearly flat line (slight decrease). This discrepancy may be due to the fact that the nonlinear viscoelastic model parameters do not have the correct temperature dependence down to -50 C. To accurately compute in this regime, additional material data is required. Also note that there is not a failure prediction at 50 C using the 125 MPa critical stress. This analysis, like those mentioned earlier, terminated before the critical hydrostatic stress was attained. However, unlike the prior elastic results, the 50 C analysis showed a substantial nonlinearity in the stress versus deflection response (being closer to glass transition). This precluded us from comfortably extrapolating the stress curve to 125 MPa to obtain an estimate of the load to fail. Once again, there is qualitatively no difference between the predictions made with a critical stress of 100 MPa and those made with a value of 125 MPa.

Finally, there are a few things to mention about the sensitivity of glassy failure to the polymer's degree of cure. Because the glass transition temperature, Tg, increases with the degree of cure, one must vary the test temperature, T, to conduct glassy failure tests at a constant value of (T-Tg). On doing that, one finds that the load and displacement to fail as well as the apparent fracture toughness of the material all go through a relative maximum. This can be seen in Figures 24 and 25. The Sandia cure schedules for encapsulated components are structured to hit that maximum. The decrease in toughness for the higher degrees of cure is attributed to the decrease in heat capacity and glassy modulus. This behavior is typical of what would be encountered in long term aging of encapsulated components, and it can be modeled. The toughening that occurs during the early stages of cure is not yet well understood.

IX. Finite Element Meshing and Modeling Issues

Finite element methods use a spatial discretization to capture the deformation gradients in a general boundary value problem. Because individual finite elements adopt limited basis functions for their representation of the deformation fields, they must be concentrated in regions of large gradients to have sufficient degrees of freedom to accurate represent the solution. In the problems under consideration, this required meshes to be refined near the notches. Even so, for the rubbery elastic analyses, the maximum stress/strain occurs on the free surface at the tip of the notch. Since the stresses are computed at the centroid of the finite elements and not at this free surface location, this means that there is always an offset between the actual maximum strain and the maximum strain in any finite element. At a crack tip, the elastic stresses are infinite and

no amount of mesh refinement can capture this local gradient. However, in non-singular geometries (such as the rounded notches chosen for this study), the local gradients are finite. This means that in principle, with sufficiently refined meshes, one can obtain solutions of specified accuracy. This is the basis for so called h-adaptive (or p-adaptive) finite element methods. Given that any failure testing has some margin of error associated with the loads or displacements to fail, it is sufficient for the finite element analyses to predict maximum stresses and strains that lie within these experimental error windows.

The finite element meshes for all of the aforementioned analyses were generated from a meshing script. Furthermore, the script was parameterized to allow geometric and meshing parameters to be changed readily and consistently. By design, these meshes were constructed to produce comparably sized finite elements for all four variations of the semi-circular notched sample (D=0.125", 0.25", 0.50", and 0.69") and for all three variations in the narrow notched specimen (a/W=0.3, 0.4, 0.5). As a result of this strategy, solutions of comparable accuracy were obtained enabling one to apply the chosen failure metric consistently to all test variations.

While it is true that accurate, non-singular, elastic finite element solutions are attainable with sufficient mesh refinement, it still can be a challenging task. For the problems under study, this is exacerbated by the fact that the rubbery epoxy is nearly incompressible, the finite element meshes contain a large spread in element sizes to cover the whole domain of the 3-point bending sample, and the solutions are obtained with codes using iterative solvers. Although these factors were considered in generating and analyzing the meshes for the problems that have been presented, there is room for additional work in obtaining and proving that highly accurate (spatially converged, h-adaptivity) solutions have been obtained. In the closing weeks of this project, additional meshing studies were performed indicating that greater accuracy is attainable. Quantitatively, this affects the magnitude of the failure metric that is chosen from the test analyses. This means for example, that the maximum strain criterion (0.24) that was identified from the prior analyses is actually a lower bound. Although better estimates can be obtained with additional mesh refinement, this qualitatively does not change the predictive capabilities of the proposed approach.

X. Summary

In the course of developing a nonlinear viscoelastic cohesive failure criterion, the following work has been performed:

- 1) Conducted three-point bending tests on notched samples to collect cohesive failure data varying temperature, loading rate and notch geometry
- 2) Hypothesized failure mechanisms for rubbery and glassy behavior
- 3) Identified consistent local failure metrics directly obtainable from finite element results
- 4) Analyzed failure tests with nonlinear viscoelastic material model and used the local failure metrics to predict failure

The physical picture of thermoset failure is different for rubbery and glassy behavior. Rubbery failure seems to be controlled by the finite extensibility of the network chains, and glassy failure appears to involve a cavitation event. Based on these assumptions, local failure metrics were proposed. For the rubber, a local metric based on the maximum strain correlates well with the observed failures. For the glass, a local metric based on the maximum hydrostatic tensile stress seems to work. Both criteria involve parameters readily attainable from nonlinear viscoelastic finite element analyses.

XI. Future Direction

This work provides a good foundation for understanding cohesive failure by demonstrating the feasibility of using local finite element results to define metrics which correlate with glassy and rubbery failure mechanisms in thermosets. However, there is a strong need to check the consistency of the local failure metrics in more complicated geometries and loading scenarios. One such example might be to study and predict cohesive failures around corners in an encapsulated inclusion. If the methodology is found to work in general, then these criteria should be implemented directly in our finite element codes for use in polymer analyses (e.g., encapsulation failure).

XII. References

- 1) Broek, David, *Elementary Engineering Fracture Mechanics*, 3rd ed., Martinus Nijhoff, The Hague, 1982.
- 2) Blanford, Mark, "JAS3D: A Multi-Strategy Iterative Code for Solid Mechanics Analysis Users' Instructions Release 1.6F", Sandia National Laboratories/NM, memo to distribution dated 9/14/99.

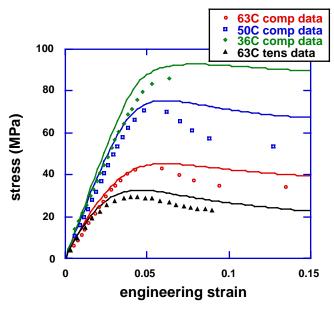


Figure 1. Nonlinear viscoelastic stress-strain data and predictions under uniaxial compression/tension conditions at different temperatures.

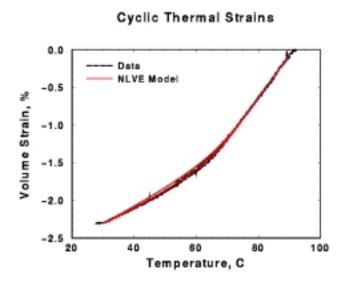


Figure 2. Nonlinear viscoelastic data and predictions of volume straining under cyclic cooling and heating at 2 C/min.

Heat Capacity Validation Tests

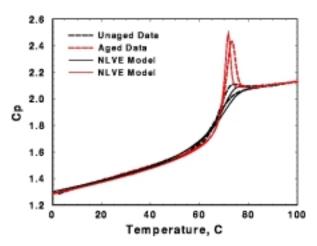


Figure 3. Nonlinear viscoelastic data and predictions of constant pressure heat capacity from enthalpy relaxation on both aged and unaged samples.

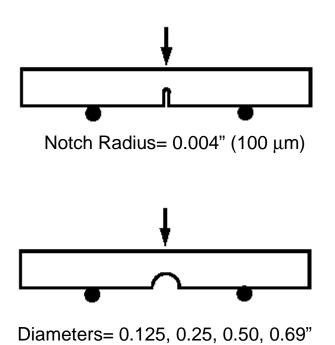


Figure 4. Notched beam geometries for 3-point bending failure tests.

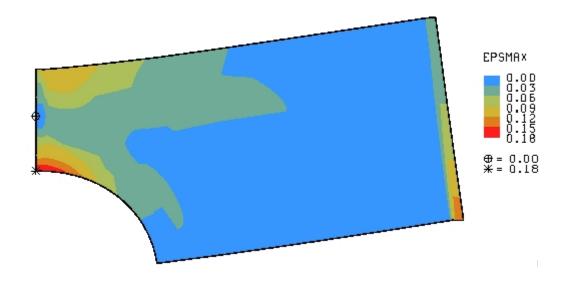


Figure 5. Maximum strain plot from rubbery elastic analysis of semi-circular notched (D=0.50") three-point bend sample.

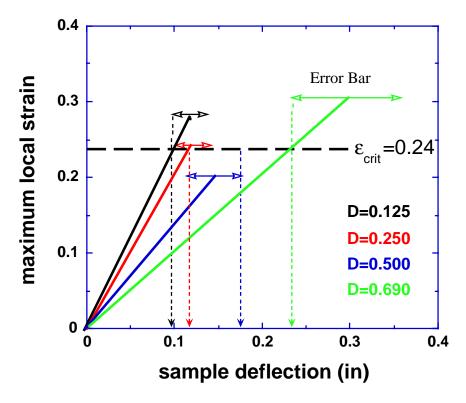


Figure 6. Growth in maximum strain with mid-span deflection during three-point bending rubbery failure tests on semi-circular notched samples.

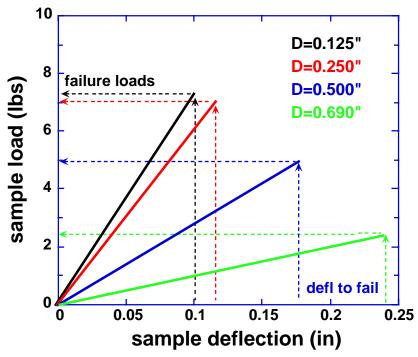


Figure 7. Variation in sample load with mid-span deflection during three-point bending rubbery failure tests on semi-circular notched samples.

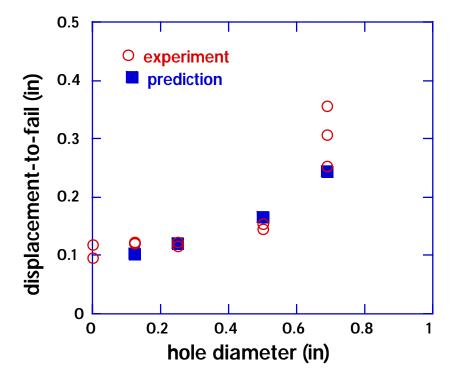


Figure 8. Variation in displacement to fail with hole diameter during three-point bending rubbery failure tests on semi-circular notched samples.

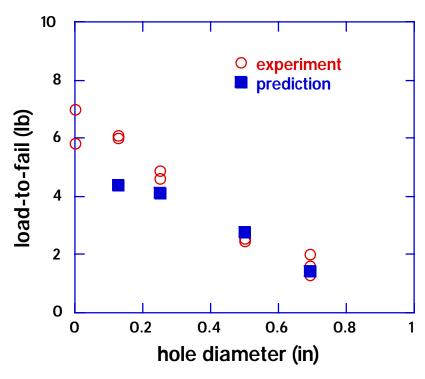


Figure 9. Variation in load to fail with hole diameter during three-point bending rubbery failure tests on semi-circular notched samples.

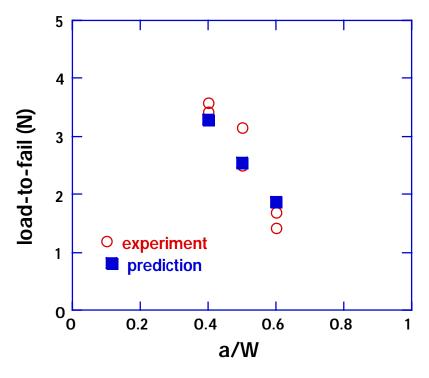


Figure 10. Variation in load to fail with a/W ratio during three-point bending rubbery failure tests on narrow-notched samples.

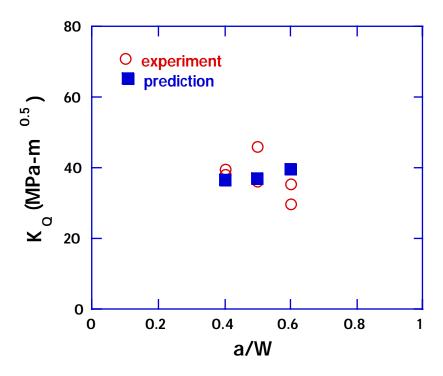


Figure 11. Variation in apparent fracture toughness with a/W ratio during three-point bending rubbery failure tests on narrow-notched samples.

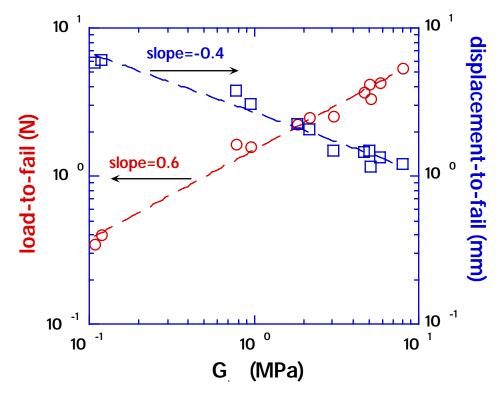


Figure 12. Effect of rubbery shear modulus on load and displacement to fail obtained from rubbery failure tests.

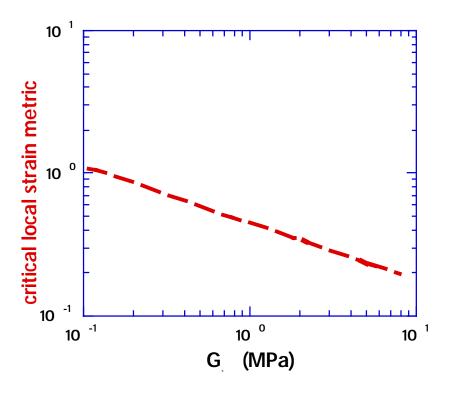


Figure 13. Effect of rubbery shear modulus on critical failure strain used as the finite extensibility rubbery failure metric.

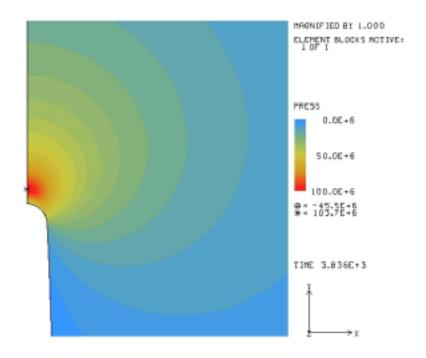


Figure 14. Plot of maximum hydrostatic tensile stress in notched, three-point glassy bending test.

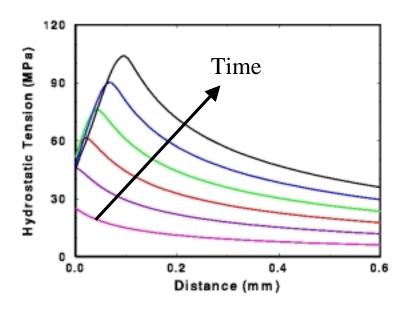


Figure 15. Variation of maximum hydrostatic tensile stress as a function of distance measured from the notch at increasing times during the glassy failure test.

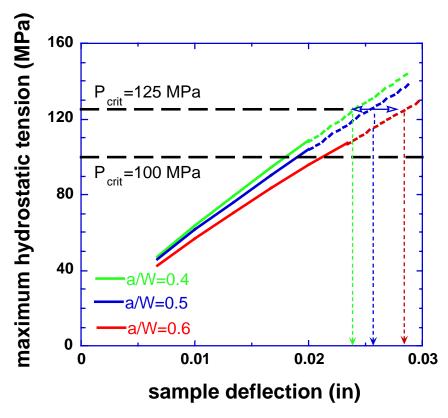


Figure 16. Plots of the maximum hydrostatic tensile stress as a function of midspan deflection for the glassy failure test with the narrow-notched sample.

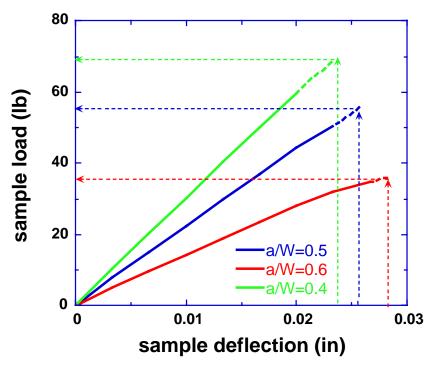


Figure 17. Plots of the load versus mid-span deflection for the glassy failure test with the narrow-notched sample.

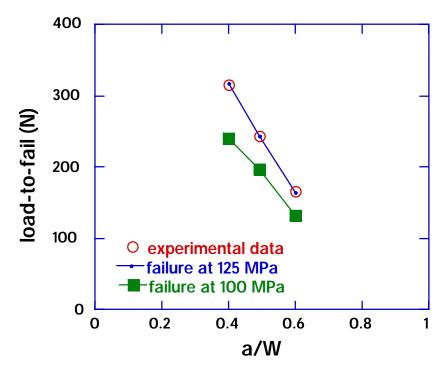


Figure 18. Plots of the data and the predicted load to fail as a function of the a/W ratio for the glassy failure tests with the narrow-notched sample using two different critical failure metrics.

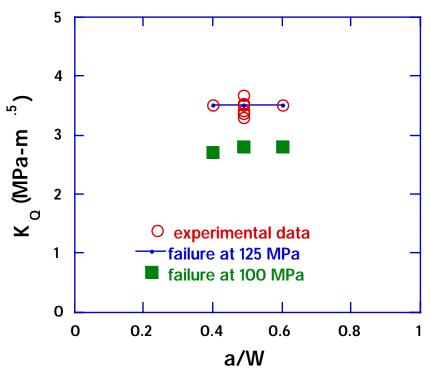


Figure 19. Plots of the apparent toughness as a function of the a/W ratio for the glassy failure tests with the narrow-notched sample using two different critical failure metrics.

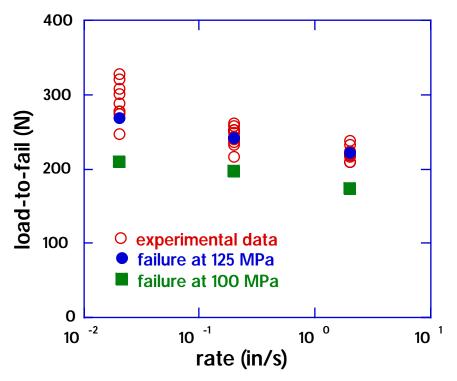


Figure 20. Plots of the data and predicted load to fail as a function of the deflection rate for the glassy failure tests with the narrow-notched sample using two different critical failure metrics.

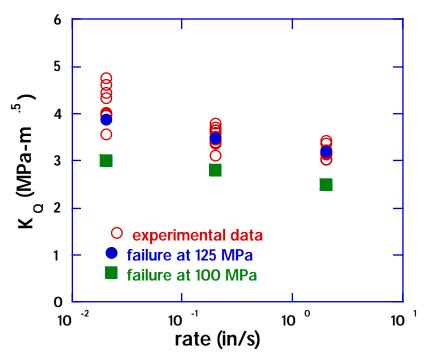


Figure 21. Plots of the apparent toughness as a function of the deflection rate for the glassy failure tests with the narrow-notched sample using two different critical failure metrics.

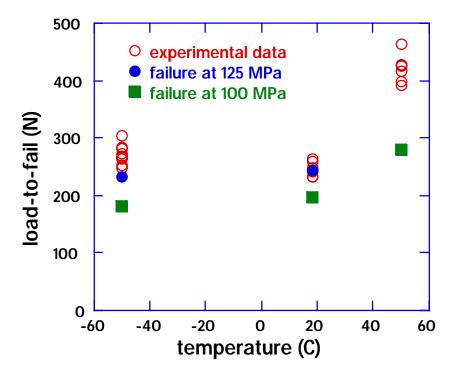


Figure 22. Plots of the data and the predicted load to fail as a function of temperature for the glassy failure tests with the narrow-notched sample using two different critical failure metrics.

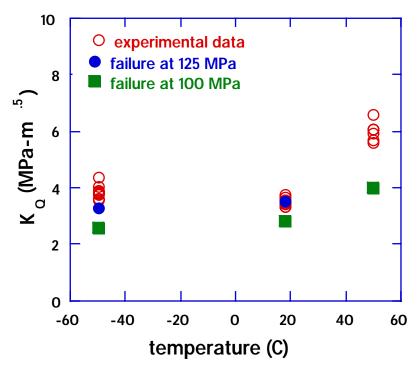


Figure 23. Plots of the apparent toughness as a function of temperature for the glassy failure tests with the narrow-notched sample using two different critical failure metrics.

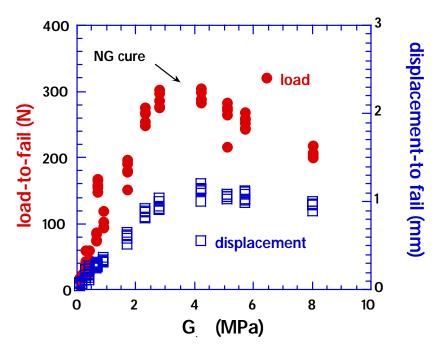


Figure 24. Plots of the load and displacement to fail as a function of rubbery shear modulus (varying degree of cure) for glassy failure tests.

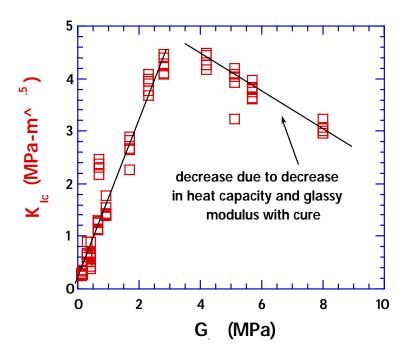


Figure 25. Fracture toughness as a function of rubbery shear modulus (varying degree of cure) for glassy failure tests.

Appendices

Appendix A Fracture Toughness of 828/DEA Epoxy-Effects of Loading Rate and Test Temperature

Tommy Guess and Mark Stavig, 1472 January 1998

This preliminary test report summarizes fracture toughness and dynamic mechanical analyzer (DMA) data for unfilled 828/DEA epoxy that has been generated for our LDRD "Micromechanical Failure Analyses for Finite Element Polymer Modeling".

Material

The epoxy formulation, cure schedule and annealing schedule used are listed in Table 1.

ENCAPSULANT

MIX RATIO (pbw)

CURE SCHEDULE

ANNEALING SCHEDULE

(just prior to fracture tests)

ENCAPSULANT

828/DEA

100/12

90C for 24 hours

15 minute ramp RT to 90C

20 minute hold at 90C

2C/min ramp 90C to RT

Table 1 Material Tested

Specimens were annealed prior to testing to remove thermal history and get them all in the same condition. The fracture toughness specimens were annealed after the crack was introduced. It is of interest to note that the crack could be seen visually prior to the annealing process, but not after annealing. The small glitch observed early in most of the loading curves is thought to be tied to fact that somehow the annealing somehow affects the initial opening of the crack.

Fracture Toughness Tests

Plane strain fracture toughness K_{IC} of the Epon 828/DEA epoxy was measured using an edge-cracked, three-point bend specimen with a support span of 2 inches. Testing procedures followed the guidelines in ASTM E-399, the Standard Test Method for Plane-Strain Fracture Toughness of Metallic Materials. A sharp crack of length 'a' was introduced on one edge of a cast, rectangular bar (length = 4", depth w = 0.5", and thickness = 0.25"). The procedure to produce the crack was 1) saw a narrow slot about 0.1" deep, 2) scribe a line with a razor blade onto the bottom of the saw cut, 3) clamp the sample in a cracking fixture, and 4) lightly tap the razor blade located on the scribed line to grow a sharp crack to a length-to-depth ratio of a/w = 0.3 to 0.7.

Tests were done at three temperatures and three crosshead rates. The effect of loading rate was probed by using three loading rates (0.02, 0.2, and 2.0 in/min) at room temperature (23C); and the effect of temperature was investigated by using three temperatures (-60C, 23C and 50C) at one loading rate (2.0 in/min). The original intent was to use 0.2 in/min but there was too much

yielding during the 50C tests. Therefore, the loading rate was increased to 2 in/min for the temperature effect tests. A minimum of 8 specimens were tested at each condition.

Typical load versus time responses as a function of test temperature are shown in Figure 1. At the 2 in/min loading rate, it takes less than 0.4s to load to failure. On the other hand, it takes up to about 25s when the loading rate is 0.02 in/min (see Figure 2).

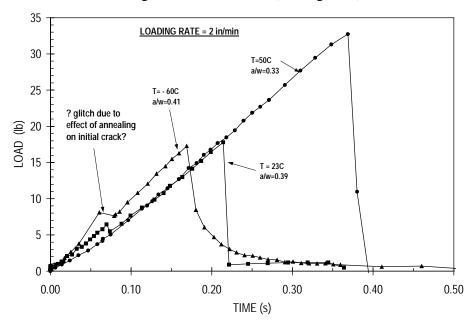


Fig. 1. Comparison of time to fracture for three temperatures at a loading rate of 2 in/min.

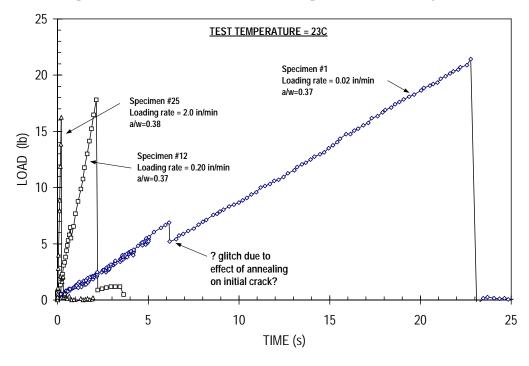


Fig. 2. Comparison of time to fracture for three loading rates at a test temperature of 23C.

Fracture toughness values are listed in Table 2; the average and standard deviation of each data set is plotted in Figure 3.

Sample	Test Temperature		Ratio Crack length / Sample Depth	Fracture Toughness K _{IC}	
ID	(C)	(in/min)		(psi-in ^{.5})	
			ng Rate (at constant test ter		
#1	23	0.02	0.368	894	
#2	23	0.02	0.449	799	Λνα
#3	23	0.02	0.334	1032	Avg = ₉₄₀ Stdev = ₈₇
#4	23	0.02	0.684	1059	Staev = 87
#6	23	0.02	0.443	895	cv (%) = 9.3
#7	23	0.02	0.539	991	
#8	23	0.02	0.382	883	
#9	23	0.02	0.374	969	
#10	23	0.2	0.349	783	
#11	23	0.2	0.328	846	
#12	23	0.2	0.366	761	
#13	23	0.2	0.317	697	Avg = 787
#14	23	0.2	0.397	817	Stdev = 44
#15	23	0.2	0.337	750	cv (%) = 5.6
#16	23	0.2	0.634	772	
#17	23	0.2	0.320	830	
#18	23	0.2	0.367	815	
#19	23	0.2	0.325	800	
#20	23	2.0	0.663	768	
#21	23	2.0	0.389	677	
#22	23	2.0	0.429	750	Avg = 711
#23	23	2.0	0.345	674	Stdev = 31
#24	23	2.0	0.510	708	CV (%) = 4.4
#25	23	2.0	0.378	704	CV (70) - 4.4
#26	23	2.0	0.669	722	
#27	23	2.0	0.346	700	
#28	23	2.0	0.464	700	
			emperature (at constant loa		
-60C #1	-60	2.0	0.696	774	
-60C #2	-60	2.0	0.345	794	
-60C #3	-60	2.0	0.360	790	Δισ
-60C #4	-60	2.0	0.461	824	Avg = 794 Stdev = 48
-60C #5	-60	2.0	0.411	820	Sidev = 48
-60C #6	-60	2.0	0.353	735	cv (%) = 6.0
-60C #7	-60	2.0	0.500	764	
-60C #8	-60	2.0	0.392	722	
-60C #9	-60	2.0	0.352	885	
60C #10	-60	2.0	0.380	823	
60C #11	-60	2.0	0.476	781	
#20	23	2.0	0.663	768	
#21	23	2.0	0.389	677	
#22	23	2.0	0.429	750	
#23	23	2.0	0.345	674	Avg = 711
#24	23	2.0	0.510	708	Stdev = 31
#25	23	2.0	0.378	704	CV (%) = 4.4
#26	23	2.0	0.669	704	(/ 4.4
#27	23	2.0	0.346	700	
	23 23		0.464	700 700	
#28		2.0			
50C-2	50	2.0	0.450	1156	
50C-3	50	2.0	0.330	1239	
50C-4	50	2.0	0.546	1205	Avg = 1224
50C-5	50	2.0	0.369	1138	Stdev = 63
50C-6	50	2.0	0.629	1344	cv (%) = 5.1
50C-7	50	2.0	0.388	1232	
50C-8	50	2.0	0.560	1236	
50C-9	50	2.0	0.385	1238	

Table 2. 828/DEA Fracture Toughness Data

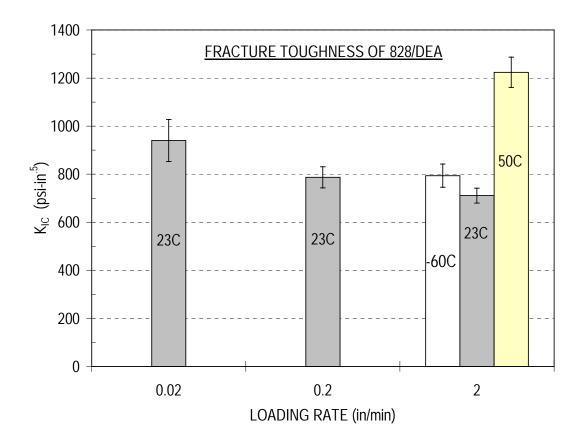


Fig. 3. K_{IC} Fracture Toughness of 828/DEA as a function of test temperature and loading rate. Data are averages and error bars are one standard deviation.

The effect of loading rate at temperatures near $T_{\rm g}$ is shown in Figure 4.

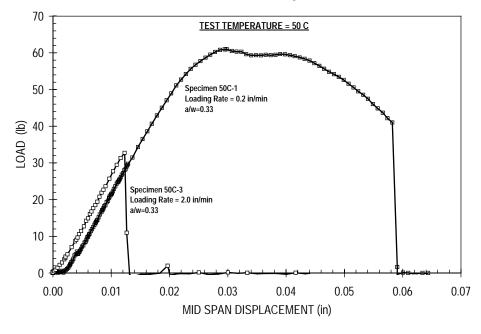


Fig. 4. Comparison of load vs displacement characteristics of 828/DEA near $T_{\rm g}$ at two loading rates. The test at 0.2 in/min is not valid for fracture toughness calculations because of large scale yielding.

DMA Tests

A thin plaque of 828/DEA was processed at the same time the fracture toughness specimens were poured. Strips from the plaque were used in torsional DMA tests to measure the glass transition temperature T_g of the epoxy; typical DMA data are plotted in Figure 5. Tg has a value of ~71C if taken as the onset of the glassy-to-rubbery response and ~83C if taken as the temperature at the peak of the Tan δ response.

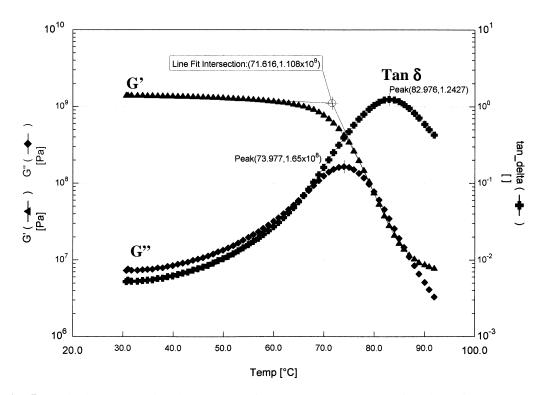


Fig. 5. Typical DMA torsional test results for 828/DEA epoxy as a function of temperature.

Appendix B Rigid Square Inclusion Embedded within an Epoxy Disk: Asymptotic Stress Analysis

E. D. Reedy, Jr. and T. R. Guess

Sandia National Laboratories, Albuquerque, New Mexico 87185

Abstract

The asymptotically singular stress state found at the tip of a rigid, square inclusion embedded within a thin, linear elastic disk has been determined for both uniform cooling and an externally applied pressure. Since these loadings are symmetric, the singular stress field is characterized by a single stress intensity factor K_a, and the applicable K_a calibration relationship has been determined for both a fully bonded inclusion and an unbonded inclusion with frictionless sliding. A lack of interfacial bonding has a profound effect on inclusion-tip stress fields. When the inclusion is fully bonded, radial compression dominates in the region directly in front of the inclusion tip and there is negligible tensile hoop stress. When the inclusion is unbonded the radial stress at the inclusion tip is again compressive, but now the hoop tensile stress is of equal magnitude. Consequently, an epoxy disk containing an unbonded inclusion appears more likely to crack when cooled than a disk containing a fully bonded inclusion. Elastic-plastic calculations show that when the inclusion is unbonded, encapsulant yielding has a significant effect on the inclusion-tip stress state. Yielding relieves stress parallel to the interface and greatly reduces the radial compressive stress in front of the inclusion. As a result, the encapsulant is subjected to a nearly uniaxial tensile stress at the inclusion tip. For a typical high-strength epoxy, the calculated yield zone is embedded within the region dominated by the elastic hoop stress singularity. A limited number of tests have been carried out to determine if encapsulant cracking can be induced by cooling a specimen fabricated by molding a square, steel insert within a thin, epoxy disk. Test results are in qualitative agreement with analysis. Cracks developed only in disks with mold-released inserts, and the tendency for cracking increased with inclusion size.

Introduction

Polymeric encapsulants are widely used in the automotive, aerospace, and electronic industries. The encapsulant holds a component in place and protects it from applied loads and the surrounding environment. If the encapsulant cracks the component may fail. In many cases the encapsulated part has sharp corners. For example, sharp corners are often found in microelectronic chip packages. When failure occurs, it will typically initiate at a corner. On a finer scale, polymer encapsulants are usually filled with particles to improve their properties. Some common types of fillers are created by crushing a bulk material, and as a consequence, the filler has sharp corners. Microcracks initiating at sharp-cornered particles can degrade a filled material.

A simple, 2-D idealization of an encapsulated sharp-cornered component or particle is a homogeneous, isotropic, square inclusion embedded within an isotropic material (Fig. 1). The encapsulated component or particle is typically much stiffer than the encapsulant, and it is often reasonable to regard the inclusion as rigid. When viewed asymptotically, the inclusion tip is the apex of a wedge (Fig. 2). Several studies have provided detailed information about the stress field found at the tip of a linear elastic wedge. Williams (1952) analyzed a single material wedge with a variety of edge boundary conditions. He noted that a power-law stress singularity

$$\sigma \sim K_a r^{\lambda - 1} - 1 < \operatorname{Re}(\lambda - 1) < 0 \tag{1}$$

can exist at the apex of the wedge and determined how the order of the stress singularity, λ -1, depends on boundary conditions and elastic properties. For singular stress and bounded displacements, $-1 < \text{Re}(\lambda - 1) < 0$, Williams' results for a wedge with both edges clamped are applicable to a rigid inclusion surrounded by an elastic material. Bogy and Wang (1971) analyzed bonded, dissimilar elastic wedges that together form a full plane. These results show how the strength of the stress singularity depends on the elastic properties of the inclusion. Chen and Nisitani (1993) noted that there are at most two power-law singular terms in the asymptotic expansion of the stress field with $-1<\lambda-1<0$ for many cases of practical interest (when $\beta(\alpha-\beta)>0$, where α , β are the elastic bimaterial parameters defined by Dundurs, 1969). The exponent defining the strength of each of the singular terms is real, and the two exponents are generally different. They also found that one of the singular terms is associated with symmetric loading about the line bisecting the apex of the wedge, whereas the other is associated with an asymmetric loading about the bisecting line (i.e., x axis in Figure 2). In another study Chen (1994) presented stress intensity factor relations for a bonded inclusion embedded within an infinite plate subjected to uniaxial tension, biaxial tension, or shear at infinity. A variety of inclusion shapes were considered.

The value of the stress intensity factor K_a (Eq. 1) characterizes the magnitude of the stress state in the region of the inclusion tip (the subscript "a" on K is used to denote that this stress intensity factor is associated with the apex of a wedge). It is reasonable to hypothesize that failure occurs at a critical K_a value, K_{ac} . Such an approach is analogous

to linear elastic fracture mechanics, except here the critical value of the stress intensity factor is associated with a discontinuity other than a crack. As is the case of linear elastic fracture mechanics, small-scale yielding conditions must apply. The asymptotic stress state characterized by K_a must dominate a region that is significantly larger than the fracture process zone, plastic yield zone, and the extent of any subcritical cracking. The inclusion tip must also appear sharp on this length scale.

The applicability and accuracy of a K_a-based failure analysis to encapsulated inclusions has yet to be conclusively demonstrated. There appear to be few published experimental results applying this approach to encapsulated bodies. One exception is the work of Hattori et al (1989), who molded epoxy models with small Fe-Ni inserts and looked for failure as the molding cooled. Note, however, there is convincing evidence that the stress intensity factor for other types of corner discontinuity can be used to predict failure. Reedy and Guess (1993, 1995, 1996a, 1997, and 1999) have shown that the observed reduction in the tensile strength of adhesively-bonded, cylindrical butt joints, with increasing bond thickness, is accurately predicted by a K_{ac} criterion. In this case K_{ac} is associated with an interface corner, the point where the interface between two bonded quarter planes intersects the stress-free edge. Dunn et al, (1997a, b) have successfully predicted the fracture of homogenous materials containing a sharp notch using a similar approach.

Reported below is the K_a calibration for a rigid, square inclusion embedded within a thin disk and subjected to either a uniform cooling or to an external applied pressure. This symmetrically loaded configuration is a particularly attractive test specimen, since the asymptotic stress field is characterized by a single K_a . Two extremes in bonding are considered: fully bonded and unbonded with frictionless sliding. Elastic-plastic calculations for a representative epoxy encapsulant have also been carried out. These results illustrate the effect of yielding on inclusion-tip stress fields and also the validity of the small-scale yielding assumption. Finally, the results of a limited number of preliminary experiments are presented.

Asymptotic Solutions for Bonded and Unbonded Inclusions

Figure 1 shows the encapsulated-inclusion geometry analyzed. A rigid, square inclusion, with side length h, is embedded within a disk of diameter D. The disk is presumed thin relative to the characteristic inclusion dimension h, and a plane stress analysis is applied. Figure 2 shows the associated asymptotic problem. Note that there is geometric symmetry about the x axis and that the uniform cooling and applied pressure loadings considered in this study are also symmetric about the x-axis. Accordingly, the line bisecting the apex of the wedge (i.e., x-axis) is a line of symmetry. Furthermore, for plane stress and with the elastic encapsulant (with Young's modulus E and Poisson's ratio v) taken to be Material 1 and the rigid inclusion Material 2, Dundurs' (1969) elastic bimaterial parameters α , β take on the values α =-1, and β =-(1-v)/2, and β (α - β)>0. Consequently, the asymptotic solution contains one singular term, and the singularity exponent is real (Chen and Nisitani, 1993, as discussed above in the Introduction).

One anticipates that the nature of the inclusion-to-encapsulant bond has a substantial effect on inclusion-tip stress fields. Typically, a strong interfacial bond is sought, although a less-than-perfect encapsulation process could thwart this desire. Even when an inclusion is initially well bonded, that bond could fail with cyclic loading or from environmental attack. For this reason asymptotic results for a fully bonded inclusion are compared with those for an unbonded inclusion (i.e., mold released) that is free to undergo frictionless slip. When the inclusion is rigid, only the one-material wedge representing the encapsulant is analyzed. The edge boundary conditions are chosen to reflect the presence of the rigid inclusion. For a bonded inclusion the wedge edges are fully fixed. For an unbonded inclusion with frictionless slip, the edges are shear-free, and only the normal displacement is fixed. Here it is assumed that for uniform cooling $(\Delta T < 0)$ or for a uniform external pressure $(P^* > 0)$, interfacial normal stress is always compressive, and there is no tendency for a gap to form at the encapsulant-to-inclusion interface (this was verified by the finite element calculation discussed below). The homogeneous boundary conditions on the edges of the wedge define an eigenvalue problem for the strength of the stress singularity, and the angular variation of the asymptotic stress field is associated with the corresponding eigenfunctions. Solutions to these types of asymptotic problems are well known (Williams, 1952; Seweryn and Molski, 1996), so only results are presented here.

Figure 3 shows that the strength of the stress singularity displays a modest dependence on Poisson's ratio when the inclusion is fully bonded. When $\nu=0.0$, $\lambda-1=-0.28$, whereas when $\nu=0.5$, $\lambda-1=-0.23$. The severity of the stress singularity decreases as Poisson's ratio increases. This can be contrasted with the case of bonded rigid and elastic quarter planes (asymptotic problem for a butt joint), where the strength of the singularity vanishes when v=0.0 and is maximum when v=0.5 (Reedy, 1990). When the inclusion is unbonded, λ -1=-0.67; and this value does not vary with Poisson's ratio. The most notable finding is the dramatic increase in the strength of the stress singularity with interfacial debonding. The rigid inclusion assumption is thought to be a reasonable representation of bimaterial combinations, such as a steel inclusion embedded within an epoxy encapsulant. Chen and Nisitani (1993) have determined the characteristic equation defining the order of the inclusion-tip stress singularity for a bonded elastic inclusion. This permits an assessment of the rigid inclusion assumption. The strength of the symmetric mode singularity for a fully bonded, square, steel inclusion (E=193 GPa, v=0.3) in epoxy (E=3.5 GPa, v=0.35) is -0.242, whereas that for a rigid inclusion is -0.250; only a 3 per cent difference.

Not only is the strength of the stress singularity altered by debonding, there is also a striking change in the angular variation of the asymptotic stress state. The spatial distribution of stress in the region dominated by the stress singularity is defined by

$$\sigma_{\alpha\beta} = K_a r^{\lambda-1} \overline{\sigma}_{\alpha\beta}(\theta) \quad (\alpha, \beta = r, \theta).$$
 (2)

The functions defining the angular variation in the asymptotic stress components, $\overline{\sigma}_{\pi}(\theta)$, $\overline{\sigma}_{\theta\theta}(\theta)$, and $\overline{\sigma}_{r\theta}(\theta)$, are plotted for a bonded (v=0.35) and an unbonded inclusion in Figs. 4 and 5, respectively. Note that the functions are normalized so that

 $\overline{\sigma}_{\theta\theta}(0^\circ)=1$. With this normalization the singular hoop stress directly in front of the inclusion tip $\sigma_{\theta\theta}(0^\circ)=K_ar^{\lambda-1}$. Figure 4 shows that when the inclusion is fully bonded, the magnitude of the radial stress in front of inclusion tip $(\theta=0^\circ)$ is much larger than the hoop stress and differs in sign. On the other hand, Figure 5 shows that when the inclusion is unbonded, hoop and radial stresses are again of opposite sign but of equal magnitude. Another indication of the profound difference in the asymptotic stress state of the bonded and unbonded inclusion is evident from a comparison of the functions defining the angular variation in pressure and effective stress (Figs. 6 and 7). Figure 6 shows that effective stress $\sigma_e=(3J_2)^{1/2}$, where J_2 is the second stress deviator invariant, is highest in front the inclusion tip, and the pressure component is roughly one third of the effective stress. When the inclusion is unbonded, the effective stress is singular but independent of angular position, and pressure is nonsingular.

Calibration for Inclusion-tip Stress Intensity Factor K_a

Both the strength of the stress singularity, λ -1, and the functions defining the angular variation in stress, $\overline{\sigma}_{\alpha\beta}(\theta)$, are fully determined by the asymptotic analysis. In contrast the inclusion-tip stress intensity factor Ka is determined by the full solution and depends on elastic properties, overall geometry, and the loading. Two axisymmetric $(\theta$ -independent) loadings are considered: uniform cooling ($\Delta T < 0$) and a uniform pressure (P*> 0) applied to the disk's outer edge. These loadings are actually related. The solution for uniform cooling can be obtained by superposing a suitably chosen constant stress state with the solution for an applied pressure. If the outer edge of the epoxy disk is fixed and the disk is subjected to a uniform temperature change ΔT , then the plane stress solution is $\varepsilon_{n} = \varepsilon_{\theta\theta} = 0$, and $\sigma_{n} = \sigma_{\theta\theta} = -E\Delta\alpha\Delta T/(1-v)$, where $\Delta\alpha$ is the differential coefficient of thermal expansion ($\Delta\alpha$ =encapsulant CTE - inclusion CTE). This solution is valid for both bonded and unbonded inclusions. The superposition of this constant stress state and the solution for a disk subjected to an edge pressure $P^*=-E\Delta\alpha\Delta T/(1-v)$ yields the solution for the uniform cooling of a disk with a stress-free edge. The pressure loading provides the fundamental singular solution, and the magnitude of the stress singularity will depend on P*, with P*= $-E\Delta\alpha\Delta T/(1-v)$ for uniform cooling.

The region dominated by the asymptotic solution can be extended by adding an asymptotically constant term, when it exists, to the singular term (Reedy, 1993). The asymptotic solution then has the form

$$\sigma_{\alpha\beta} = K_a r^{\lambda - 1} \overline{\sigma}_{\alpha\beta}(\theta) + C\delta_{\alpha\beta} \quad (\alpha, \beta = r, \theta). \tag{3}$$

The constant stress term C must satisfy the asymptotic boundary conditions and for simple cases is readily determined. For example, consider a uniformly cooled encapsulant bonded to a rigid inclusion. If the encapsulant were unbonded, its in-plane area would change with a change in temperature (i.e., free thermal expansion). In a plane stress analysis, the stress state $\sigma^* = \sigma_{rr} = \sigma_{\theta\theta} = -E\Delta\alpha\Delta T/(1-\nu)$ produces an area change that precisely negates that of the thermal expansion. Consequently, this constant stress state satisfies the asymptotic problem of a uniformly cooled encapsulant bonded to a rigid

inclusion (fixed edges) since the total strain is zero. Yang and Munz (1995) have determined the asymptotic constant stress term for the more general case of a two-material elastic joint subjected to a uniform temperature change, and their result reduces to that presented here for the rigid inclusion.

Based upon dimensional considerations and the required linear dependence on load, the inclusion-tip K_a calibration relation must have the form

$$K_{a} = \sigma^{*} h^{1-\lambda} I_{p}(\nu, \frac{D}{h}), \qquad (4)$$

where

$$\sigma^* = \begin{cases} P^* & \text{uniform applied pressure } P^* \\ \frac{-E\Delta\alpha\Delta T}{1-v} & \text{uniform temperature change } \Delta T, \end{cases}$$
 (5)

whereas the asymptotically constant term is

$$C = \begin{cases} \frac{-E\Delta\alpha\Delta T}{1-\nu} & \text{bonded rigid inclusion} \\ -P^* & \text{unbonded rigid inclusion.} \end{cases}$$
 (6)

Note that for a bonded inclusion, C=0 when ΔT =0 and P* \neq 0, whereas for an unbonded inclusion, C=0 when P*=0 and $\Delta T \neq$ 0. The function I_p depends on nondimensional material and geometric parameters, and for this problem the only possibilities are ν and D/h. The value of I_p for ν and D/h combinations of interest can be determined by matching asymptotic and full field, finite element solutions.

Figure 8 shows a typical mesh used in the finite element calculations. Only one eighth of the disk (Fig. 1) is analyzed. The loading is symmetric, and there is geometric symmetry about the x and y axes as well as about the two lines that divide the square inclusion into four smaller squares. Bonded and unbonded inclusions are modeled by applying the appropriate boundary conditions to the wedge edge. A highly refined mesh is used in the region of the inclusion tip (smallest element/h=1.4e-5) to ensure an accurate match with the asymptotic solution. The mesh is composed of four-noded, plane stress elements. A calculation must be carried out for every v and D/h combination of interest

(h and σ^* can be arbitrarily chosen). For the case of the unbonded inclusion, hoop stress along the x-axis is used to calculate K_a (Eq. 3), and then Eq. 4 is used to determine I_p . When the inclusion is bonded, the magnitude of the radial stress component along the x-axis is significantly higher than that of the hoop component (Fig. 9). Consequently when the inclusion is bonded, the radial stress along the x-axis (with the asymptotic constant term that exists in this case subtracted out) is used to calculate K_a and I_p . Table 1 lists λ -1 and I_p values for a range of ν and D/h. Note that results for the unbonded inclusion display only a minimal dependence on D/h for D/h>5. For this range of D/h, the stress state is essentially independent of D (i.e., disk acts as if its infinite).

For sufficiently large D/h it seems likely that the stress state developed in regions far from the inclusion will not depend on inclusion shape. The stresses are expected to approach those found in a disk containing a circular inclusion of equal area. Specifically for r>>h, one anticipates for plane stress

$$\sigma_{\rm rr} = -\sigma_{\theta\theta} = \frac{E\Delta\alpha\Delta T}{1+v} \left(\frac{r_{\rm o}}{r}\right)^2, \text{ where } r_{\rm o} = \frac{h}{\sqrt{\pi}}.$$
 (7)

Comparison of Full and Asymptotic Solutions

The results plotted in Figs. 9 and 10 illustrate the nature of inclusion-tip stress fields and the range of applicability of the asymptotic solutions. These results are for a disk with diameter D=127 mm and for an inclusion with side length h=18 mm (D/h=7). The disk is subjected to uniform cooling with ΔT =-100°C. Encapsulant properties are representative of a typical, high-strength epoxy. The encapsulant has a Young's modulus E=3.5 GPa, Poisson's ratio v=0.35, and $\Delta\alpha$ =40e-6/°C.

When cooled, a large radial compressive stress is generated at the tip of a bonded inclusion (Fig. 9). Although tensile, the hoop stress is relatively low. This stress state does not seem to favor encapsulant cracking. Recall that for the bonded inclusion, an asymptotically constant term exists whenever $\Delta T \neq 0$ (Eq. 6). This term must be added to the singular term to get good agreement with the finite element result. When the constant term is included, the asymptotic and finite element results for $\sigma_{rr}(0^{\circ})$ are within 4 per cent for r/h<0.056. The finite element and circular inclusion results for $\sigma_{rr}(0^{\circ})$ merge when r/h>0.2. A large tensile hoop stress is generated when a disk with an unbonded inclusion is cooled and, consequently, could promote cracking (Fig.10). The radial stress is of equal magnitude but is compressive. The asymptotic solution contains only a singular term, and it is within 4 per cent of the finite element result when r/h<0.17. When combined, the asymptotic and circular inclusion solutions provide an excellent match to the finite element solution over the full range of r/h. Since a large tensile hoop stress is generated only when the inclusion is unbonded, one might speculate that for encapsulant cracking to initiate at the tip of a well-bonded inclusion, the inclusion tip may need to first debond. Such debonding could be produced by thermal cycling or perhaps by environmental weakening of the interface.

Figures 11 and 12 illustrate the effect of encapsulant yielding on inclusion-tip stress fields. The epoxy is idealized as an elastic, perfectly-plastic material (σ_y = 74 MPa). Although this is a reasonable idealization when the temperature is sufficiently below the epoxy's glass transition temperature, T_g , epoxy actually responds in a much more complex manner. Stress relaxation data suggest that epoxies display nonlinear, stress-dependent viscoelasticity, and yielding is a manifestation of this constitutive behavior (Reedy and Guess, 1996). When the inclusion is fully bonded, the calculated yield zone is 0.013 mm long (at θ =0°, see Fig. 11). When the inclusion is unbonded, the yield zone is ten times longer (Fig. 12). Yielding substantially alters the stress state at the tip of the unbonded inclusion. Yielding relieves stress parallel to the interface and greatly reduces the magnitude of the radial compressive stress found in front of the inclusion. Consequently, the encapsulant directly in front of the inclusion is subjected to a nearly uniaxial, hoop tensile stress. Note that the yield zone is still embedded within the singular elastic field defining hoop stress and is, accordingly, characterized by K_a .

Comparison with Experiment

A limited number of encapsulated-inclusion specimens have been fabricated and tested. The primary goal was to simply determine if encapsulant cracking could be induced when cooling a reasonably sized specimen. Specimens were fabricated in a RTV mold. The inclusion was centered and then attached (using double-sided tape) to the bottom of a mold containing a 127 mm diameter, 6 mm deep cylindrical cavity. A lid, incorporating fill and bleed holes, ensured that the surfaces of the inclusion and epoxy disk were flush. An Epon 828 (digylcidyl ether of bisphenol A) cured with DEA (diethanolamine) epoxy was used for the encapsulant (100/12 mix ratio, cured for 16 hours at 70°C); and sharp-cornered, stainless steel inclusions, with an edge-length of either h=9 or 18 mm, were encapsulated. In some cases a mold release was applied to the inclusion to simulate the unbonded condition.

A liquid-nitrogen cooled environmental chamber was used to test the specimens. The specimens were cooled at a rate of 1°C/minute. Initial tests, using specimens with thermocouples mounted at several radial positions, showed that this rate produced nearly uniform cooling of the epoxy disk. Several specimens could be hung in the central part of the chamber at the same time. The temperature at crack initiation was determined by observing the specimens through a window in the environmental chamber. Two specimens with the larger inclusion (h=18 mm) were fabricated and tested. One specimen contained an inclusion whose edges were mold-released, whereas the other specimen contained an inclusion whose edges were subjected to a light sandblast. The specimen with the mold-released inclusion failed when first cooled to -70°C. The crack initiated from the inclusion tip. The specimen with the good interfacial bond (sandblasted edge) was cooled three separate times to -80°C and once to -140°C without encapsulant cracking. This result confirms the expectation that an unbonded inclusion promotes encapsulant cracking.

If encapsulant cracking occurs at a critical K_a value, then the temperature change required to initiate cracking decreases with increasing inclusion size (see Eq. 4).

Therefore, ten additional specimens with mold-released inclusions were fabricated. Half of these specimens contained the larger inclusion (h=18 mm) and the other half contained the smaller inclusion (h=9 mm). Three specimens of each inclusion size were cooled to -80°C, and then held at that temperature for up to three hours. Encapsulant cracking occurred in only one of the six specimens. The specimen that cracked contained the larger inclusion (h=18 mm), and cracking occurred during the -80°C hold. The four remaining specimens were first heated to 90°C (above the epoxy's T_g of 70°C), held at that temperature for about 30 minutes, and then cooled. Neither of the two specimens with the smaller inclusion cracked. On the other hand one of the specimens with the larger inclusion cracked at -105°C, and the other cracked at -135°C. In spite of the limit scope of the initial tests, the results obtained to date are in qualitative agreement with the analysis. Upon cooling, cracks developed only in disks with mold-released inclusions, and cracking occurred only in specimens with the larger inclusion.

Summary

The K_a calibration for a rigid, square inclusion embedded within a thin, epoxy disk and subjected to either a uniform cooling or to an external applied pressure has been determined. This symmetrically loaded configuration is a particularly attractive test specimen since the asymptotic stress field is characterized by a single K_a . Both fully bonded and unbonded (frictionless sliding) conditions were considered. Note that for the idealized, plane stress inclusion geometry analyzed:

- The singular stress state generated by the bonded inclusion is very different from that generated by the unbonded inclusion. For an encapsulant with a Poisson's ratio of 0.35, the strength of stress singularity for the bonded inclusion is -0.25, whereas the strength of the singularity for the unbonded inclusion is -0.67. The angular variation of the stress field also differs. When the inclusion is fully bonded, the magnitude of the radial stress in front of inclusion tip ($\theta = 0^{\circ}$, Fig. 1) is much larger than the hoop stress. When the inclusion is unbonded, hoop and radial stress have the same magnitude but are of opposite sign.
- An epoxy disk with an unbonded inclusion appears to be more likely to crack when cooled than a disk containing a fully bonded inclusion. A large radial compressive stress is generated in front of the inclusion tip when the inclusion is fully bonded, whereas a large tensile hoop stress is generated when the inclusion is unbonded. One might speculate that for encapsulant cracking to initiate at the tip of an initially well-bonded inclusion, the inclusion tip might need to first debond. Such debonding could be generated by thermal cycling or perhaps by environmental weakening of the interface.
- Encapsulant yielding has a significant effect on the nature of the stress state at the tip of an unbonded inclusion. Yielding relieves stress parallel to the interface and greatly reduces the magnitude of the radial compressive stress found in front of the inclusion. Consequently, the encapsulant directly in front of the inclusion is subjected to a nearly uniaxial, tensile stress. For a typical high-strength epoxy, the calculated yield

zone is embedded within the singular elastic field defining hoop stress and is accordingly characterized by K₂.

Results of a very limited number of tests are in qualitative agreement with the
analysis. A square, sharp-cornered steel insert was encapsulated within a thin, epoxy
disk. Upon cooling, cracks developed only in disks with mold-released inserts. The
likelihood for cracking is expected to increase with inclusion size, and only those
disks with the largest inclusion cracked.

Acknowledgment

This work was performed at Sandia National Laboratories. Sandia is a multiprogram laboratory operated by Sandia Corporation, a Lockheed Martin Company, for the United States Department of Energy under Contract DE-AC04-94AL85000. Mark Stavig performed the embedded inclusion tests.

References

Bogy, D. B., and Wang, K. C. (1971). Stress singularities at interface corners in bonded dissimilar isotropic elastic materials. *International Journal of Solids and Structures* 7, 993-1005.

Chen, D-H. and Nisitani, H. (1993). Singular stress field near the corner of jointed dissimilar materials. *Journal of Applied Mechanics* 60, 607-613.

Chen, D-H. (1994). Analysis of singular stress field around the inclusion corner tip. Engineering Fracture Mechanics 49, 533-546.

Dundurs, J. (1969). Discussion of edge-bonded dissimilar orthogonal elastic wedges under normal and shear loading. *Journal of Applied Mechanics* 36, 650-652.

Dunn, M. L., Suwito, W. and Cunningham, S. (1997a). Fracture initiation at sharp notches: correlation using critical stress intensities. *International Journal of Solids and Structures* 34, 3873-3883.

Dunn, M. L., Suwito, W., Cunningham, S. and May, C. W. (1997b). Fracture initiation at sharp notches under mode I, mode II, and mild mixed mode loading *International Journal of Fracture* 84, 367-381.

Hattori, T., Sakata, S., and Murakami, G., (1989). A stress singularity parameter approach for evaluating the interfacial reliability of plastic encapsulated LSI devices. *Journal of Electronic Packaging* 111, 243-248.

Reedy, Jr., E. D. (1990). Intensity of the stress singularity at the interface corner between a bonded elastic and rigid layer. *Engineering Fracture Mechanics* 36, 575-583.

Reedy, Jr., E. D. (1993). Asymptotic interface corner solutions for butt tensile joints. *International Journal of Solids and Structures* 30, 767-777.

Reedy, Jr., E. D. and Guess, T. R. (1993). Comparison of butt tensile strength data with interface corner stress intensity factor prediction. *International Journal of Solids and Structures* 30, 2929-2936.

Reedy, Jr., E. D. and Guess, T. R. (1995). Butt joint tensile strength: interface corner stress intensity factor prediction. *Journal of Adhesion Science and Technology* 9, 237-251.

Reedy, Jr., E. D. and Guess, T. R. (1996). Butt joint strength: effect of residual stress and stress relaxation. *Journal of Adhesion Science and Technology* 10, 33-45.

Reedy, Jr., E. D. and Guess, T. R. (1997). Interface corner failure analysis of joint strength: effect of adherend stiffness. *International Journal of Fracture*, 88, 305-314.

Reedy, Jr., E. D. and Guess, T. R. (1999). Additional interface corner toughness data for an adhesively-bonded butt joint. *International Journal of Fracture*, 98, L3-L8.

Seweryn, A. and Molski, K. (1996). Elastic stress singularities and corresponding generalized stress intensity factors for angular corners under various boundary conditions. *Engineering Fracture Mechanics* 55, 529-556.

Yang, Y. Y. and Munz, D. (1995). Stress intensity factor and stress distribution in a joint with an interface corner under thermal and mechanical loading, *Computers & Structures*, 57, 467-476.

Williams, M. L. (1952). Stress singularities resulting from various boundary conditions in angular corners of plates in extension. *Journal of Applied Mechanics* 19 526-528.

Table 1. Value of $\lambda\text{--}1$ and I_p for various ν and D/h.

Interface	ν	D/h	λ-1	$\overline{\sigma}_{rr}(0^{O})$	$\overline{\sigma}_{\theta\theta}(0^{O})$	I_p
Bonded	0.35	7.07	-0.2502	-63.25	1.00	0.0135
Unbonded	0.05	14.14	-0.6667	-1.00	1.00	0.1779
Unbonded	0.15	14.14	-0.6667	-1.00	1.00	0.1455
Unbonded	0.25	14.14	-0.6667	-1.00	1.00	0.1182
Unbonded	0.35	14.14	-0.6667	-1.00	1.00	0.0949
Unbonded	0.45	14.14	-0.6667	-1.00	1.00	0.0748
Unbonded	0.35	7.07	-0.6667	-1.00	1.00	0.0940
Unbonded	0.35	5.66	-0.6667	-1.00	1.00	0.0935
Unbonded	0.35	4.71	-0.6667	-1.00	1.00	0.0927
Unbonded	0.35	3.54	-0.6667	-1.00	1.00	0.0910
Unbonded	0.35	2.83	-0.6667	-1.00	1.00	0.0886
Unbonded	0.35	2.18	-0.6667	-1.00	1.00	0.0831

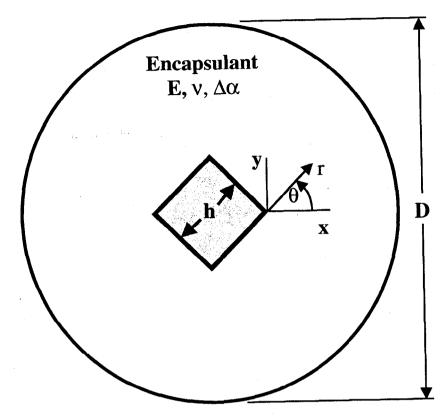


Figure 1. Rigid, square inclusion encapsulated within a linear elastic disk.

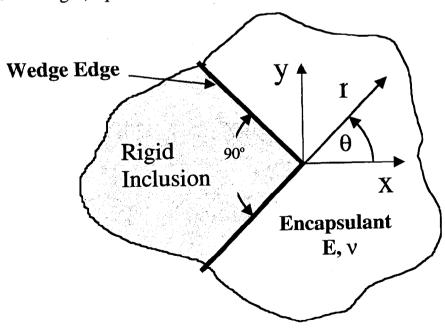


Figure 2. Asymptotic problem for encapsulated, rigid wedge. Symmetry about x axis.

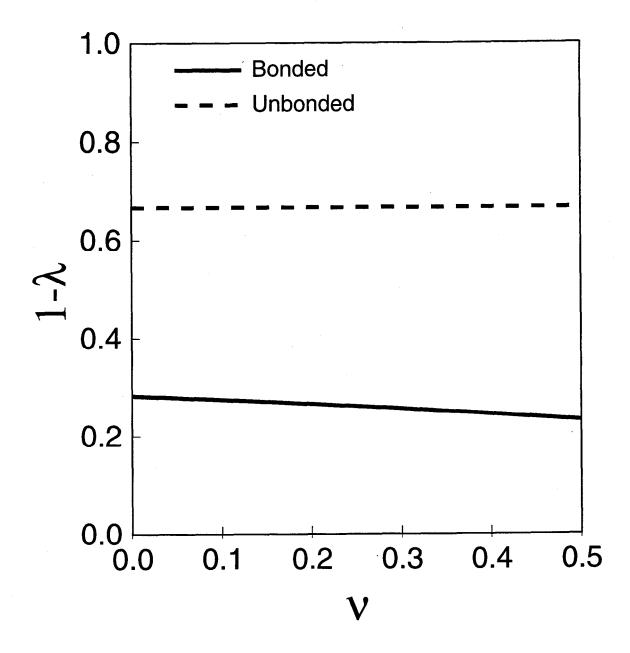


Figure 3. Variation of the strength of the stress singularity, $-(1-\lambda)$, with Poisson's ratio ν for either a bonded or an unbonded rigid square inclusion.

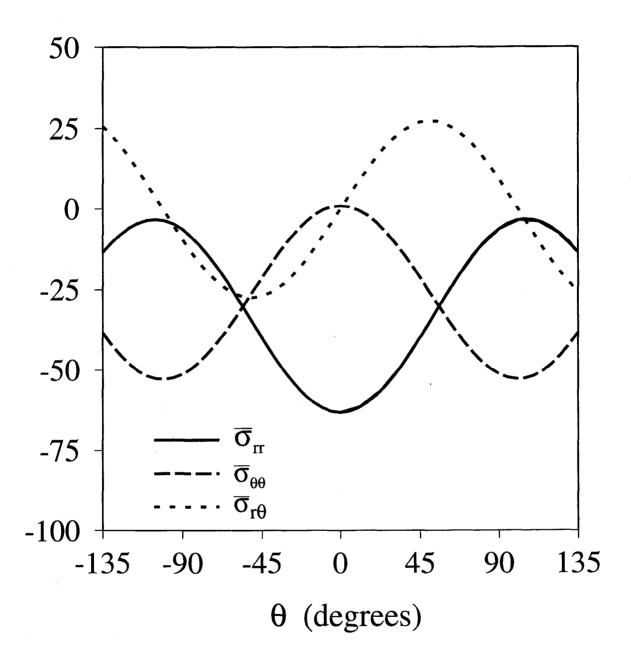


Figure 4. Angular variation of σ_{rr} , $\sigma_{\theta\theta}$, and $\sigma_{r\theta}$ about the tip of a fully bonded, rigid square inclusion (encapsulant v=0.35).

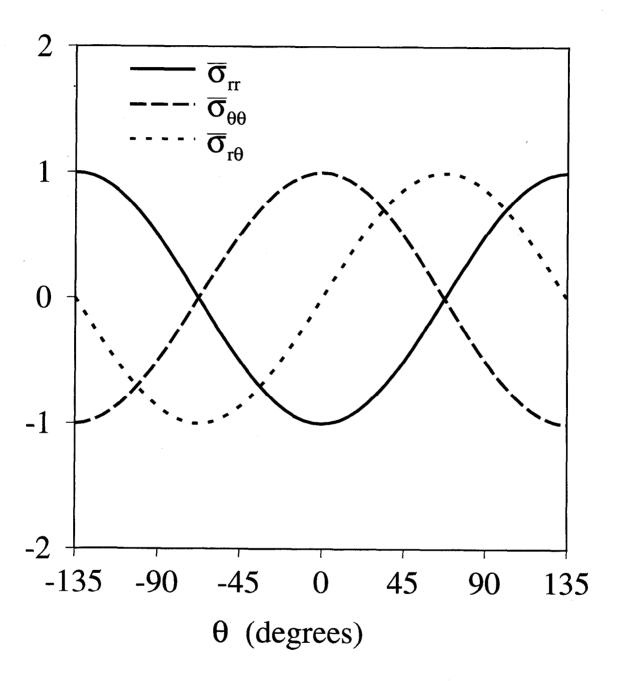


Figure 5. Angular variation of σ_{rr} , $\sigma_{\theta\theta}$, and $\sigma_{r\theta}$ about the tip of an unbonded, rigid square inclusion (frictionless sliding).

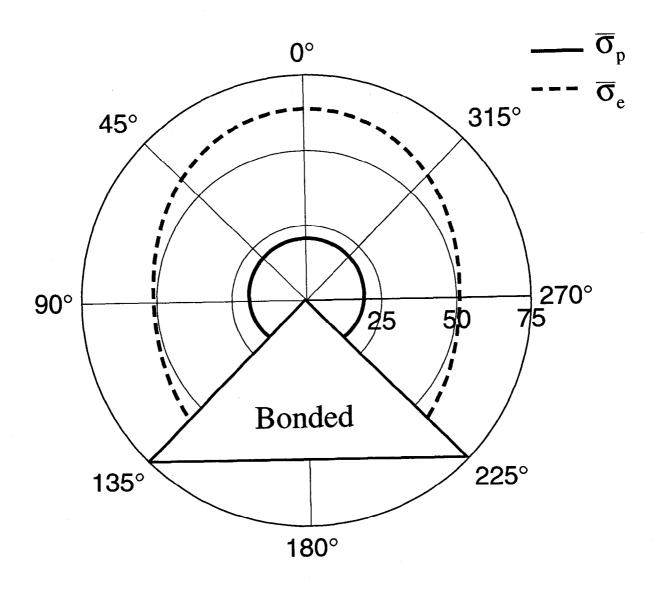


Figure 6. Angular variation of σ_p and σ_e about the tip of a fully bonded, rigid square inclusion (encapsulant v=0.35).

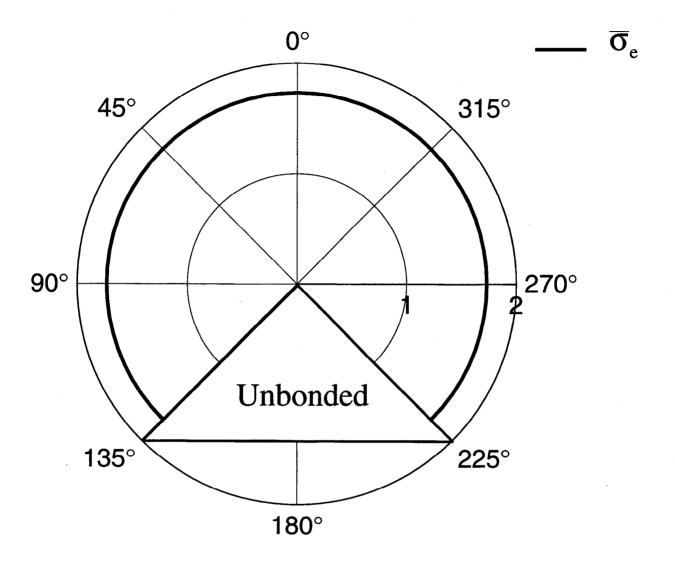


Figure 7. Angular variation of σ_e about tip of an unbonded, rigid square inclusion (frictionless sliding).

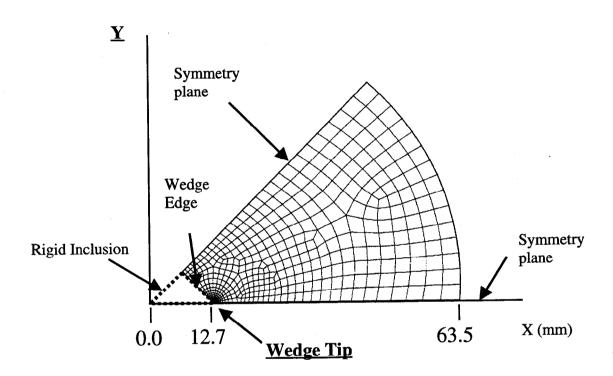


Figure 8. Typical finite element mesh used in analysis.

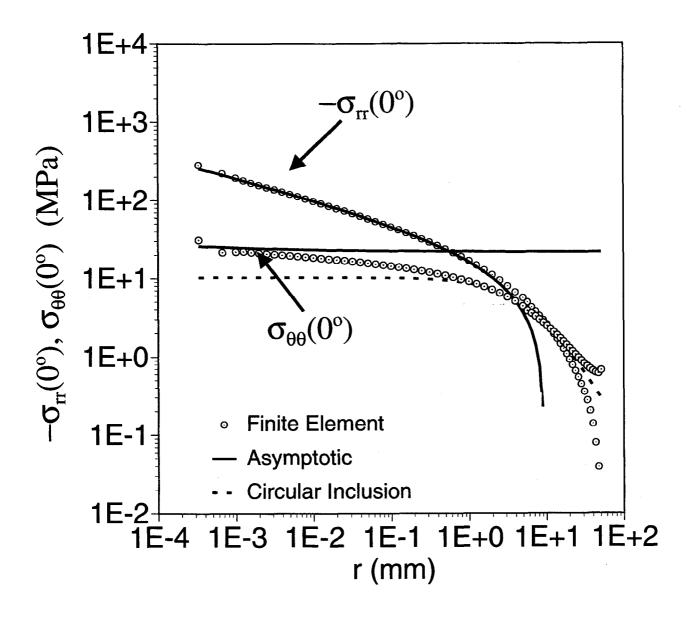


Figure 9. Comparison of linear elastic finite element and asymptotic solutions for stress in front of a fully bonded inclusion embedded within an epoxy disk with h=18mm and ΔT =-100° C.

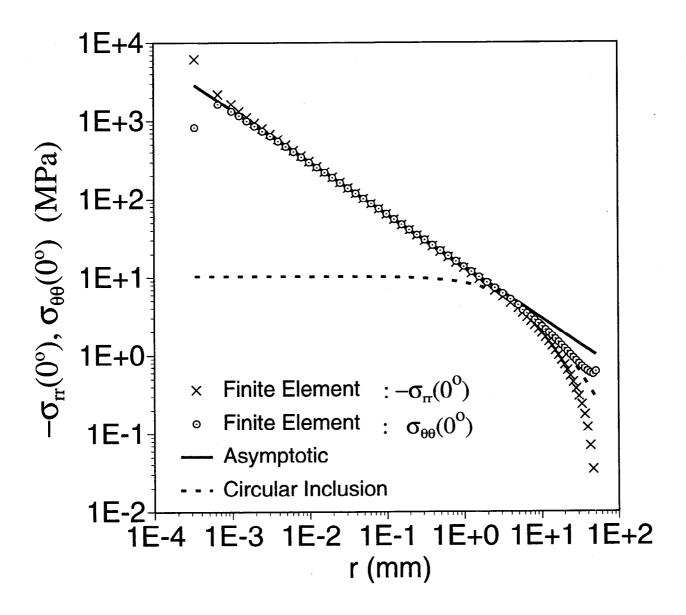


Figure 10. Comparison of linear elastic finite element and asymptotic solutions for stress in front of an unbonded inclusion embedded within an epoxy disk with h=18mm and ΔT =-100°C.

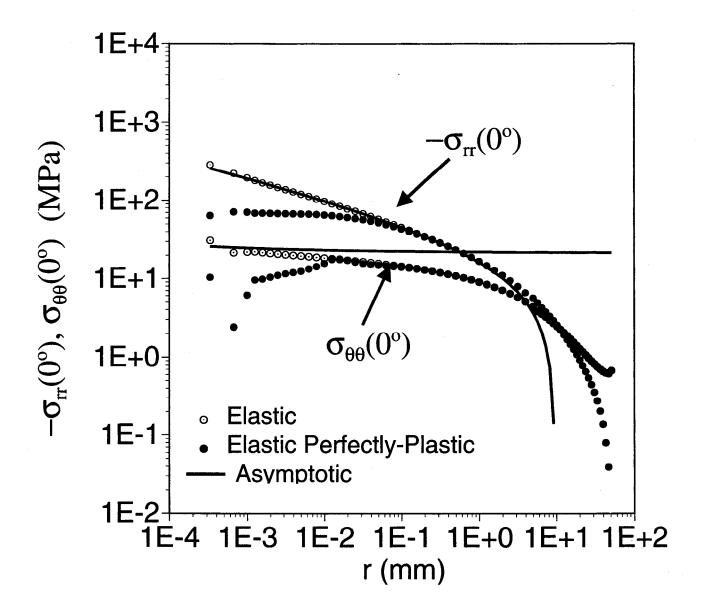


Figure 11. Comparison of linear elastic and elastic perfectly-plastic finite element solutions with asymptotic solution for stress in front of a fully bonded inclusion embedded within an epoxy disk with h=18mm and ΔT =-100°C.

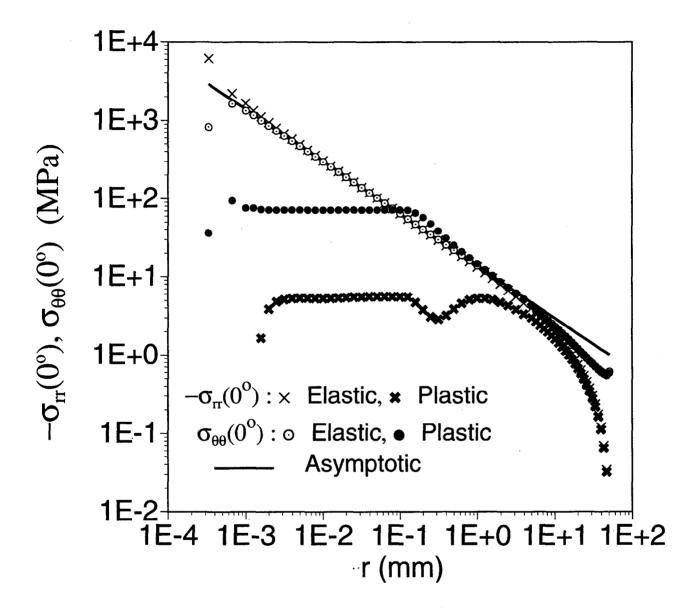


Figure 12. Comparison of linear elastic and elastic-perfectly-plastic finite element solutions with asymptotic solution for stress in front of an unbonded inclusion embedded within an epoxy disk with h=18mm and ΔT =-100°C.

Distribution List:

1	MS9018	Central Technical Files, 8945-1
2	MS0899	Technical Library, 9616
1	MS0612	Review & Approval Desk, 9612
		For DOE/OSTI
1	MS0188	LDRD Office (Donna L. Chavez)
1	MS0826	W. L. Hermina, 9113
1	MS0847	H. S. Morgan, 9123
5	MS0847	R. S. Chambers, 9123
3	MS0888	D. B. Adolf, 1811
1	MS0847	E. D. Reedy, Jr., 9123
1	MS0847	C. S. Lo, 9123
1	MS0958	T R Guess 14172